

COPY-TRANSFORM-PASTE: Zero-Shot Object-Object Alignment Guided by Vision-Language and Geometric Constraints

Rotem Gatenyo Ohad Fried

Reichman University

[GitHub](#) [Page](#)



Figure 1. **Text-guided object-object alignment and iterative composition.** The figure shows four independent examples, each presenting the input meshes and text prompt alongside our alignment result. In addition, an iterative example demonstrates progressive assembly of a burger: the output of stage k is incorporated into the input of stage $k+1$, gradually forming the final arrangement.

Abstract

We study zero-shot 3D alignment of two given meshes, using a text prompt describing their spatial relation—an essential capability for content creation and scene assembly. Earlier approaches primarily rely on geometric alignment procedures, while recent work leverages pretrained 2D diffusion models to model language-conditioned object-object spatial relationships. In contrast, we directly optimize the relative pose at test time, updating translation, rotation, and isotropic scale with CLIP-driven gradients via a differentiable renderer, without training a new model. Our framework augments language supervision with geometry-aware objectives: a variant of soft-Iterative Closest Point (ICP) term to encourage surface attachment and a penetration loss to discourage interpenetration. A phased schedule strengthens contact constraints over time, and camera control concentrates the optimization on the interaction region. To enable evaluation, we curate a benchmark containing diverse categories and relations, and compare against baselines. Our method outperforms all alternatives, yielding semantically faithful and physically plausible alignments.

1. Introduction

Objects rarely exist in isolation: everyday 3D tasks such as placing a cup on a saucer, fitting a lid on a pot or topping a sundae with a cherry, require arranging one object relative to another in a way that is both semantically intended and physically plausible. We focus on the fundamental problem of aligning two given meshes according to a short text prompt that guides the intended interaction.

Data scarcity makes this problem challenging. Unlike human-object interaction (HOI), which benefits from contact-rich datasets and evaluation protocols [5, 32], object-object interaction lacks comparable resources. Large-scale, standardized benchmarks remain limited; to our knowledge, 2BY2 [27] is the most extensive to date, yet it covers only 18 pairwise alignment tasks. This motivates a zero-shot approach that relies on pretrained models at test time rather than supervision on 3D alignment data.

To leverage vision-language signals in 3D, we expose pose parameters to image-space objectives via differentiable rendering [16, 18, 19]. Differentiable rendering provides gradients through rendering, enabling direct optimiza-

tion of explicit mesh parameters from rendered supervision [8, 12].

We use CLIP [28] as the language-vision objective: CLIP embeds text and images in a joint space, allowing us to measure cosine similarity between rendered views and the prompt. Prior 3D works have shown that CLIP supervision can drive mesh editing and stylization through rendered views [12, 20, 22]; we adopt the same supervision to inform 3D placement.

Language supervision alone does not impose contact or prevent interpenetration. Classical alignment offers complementary structure: Iterative Closest Point (ICP) aligns two shapes by alternating nearest-neighbor correspondence with a rigid pose update that minimizes point-to-point distances [4], with robust/probabilistic variants improving tolerance to noise and partial overlap [7, 23]. Building on these ideas, we introduce a *fractional soft-ICP* attachment term, our variant that applies soft correspondences only to a prescribed fraction of the closest vertices, to encourage controlled surface contact, and we add a penetration penalty to discourage interpenetration.

At test time, we perform a phased optimization that progressively increases the weights of the fractional soft-ICP and penetration terms while zooming cameras toward the interaction region; multiple random restarts with best-of- N selection improve robustness to initialization. We validate on a curated benchmark of 50 mesh-prompt pairs against geometric and LLM-based baselines, observing higher semantic agreement and lower intersection volume.

Our main **contributions** are:

1. A text-guided, test-time optimization framework that estimates the relative pose and isotropic scale between two meshes via differentiable rendering and vision-language supervision, augmented with fractional soft-ICP and penetration objectives for physical plausibility.
2. A benchmark of 50 language-conditioned mesh-pair cases for standardized evaluation of object-object alignment (OOA), against which we demonstrate consistent improvements over multiple baselines.

2. Related Work

Classical alignment and mesh composition. Rigid alignment of two shapes is commonly solved with ICP: starting from an initial pose, the algorithm alternates (i) establishing correspondences between samples on the source and target and (ii) estimating the rigid transform that best fits those correspondences, iterating to convergence [4, 7]. Other ICP formulations cast correspondence as a probabilistic assignment, such that each source sample matches multiple targets with weights; this increases robustness to noise, partial overlap, and outliers [7, 23]. Building on these primitives, interactive composition systems apply ICP within user-guided pipelines to assemble parts and enforce con-

tact; a representative example is SnapPaste [30], which performs cut-and-paste composition with contact-aware snapping. Beyond these representatives, there is a large body of ICP variants and comparisons; see, e.g., Rusinkiewicz and Levoy [29] and Tam et al. [33] for analyses of efficient ICP variants and 3D registration. These methods focus on geometric consistency and interaction cues, but do not inject semantic guidance from language or images.

Text-guided optimization with vision-language models. A large body of text-guided content synthesis is driven by CLIP [28], a foundational model that learns a joint embedding space for text and images. Optimization under CLIP guidance has proven to be effective for semantic control in images [11, 17, 25] and vector sketches [10, 31, 36]. In 3D, text-driven optimization has been used to steer shape generation directly from language [14, 26]. These methods demonstrate that language priors can guide optimization toward semantically meaningful configurations.

Optimization on 3D meshes with differentiable rendering. Other works adopt surface-based differentiable rendering to render explicit meshes and pass those views to vision-language models, enabling gradients from language-image objectives to propagate back to 3D parameters [16, 18, 19]. Within this setup, Text2Mesh [20] performs text-driven stylization of mesh appearance and local geometry, TextDeformer [12] manipulates mesh geometry under text guidance, and recent editing methods such as Chen et al. [8] and PrEditor3D [9] support controlled, localized edits. These advances can be leveraged for object-object interaction, where the goal is not to alter geometry but to recover a plausible pose between two meshes under a text prompt.

In contrast to pipelines that rely purely on geometry and to language-driven editing methods that modify shape or appearance, we address zero-shot rigid pose and scale alignment between a given pair of meshes from a text prompt, coupling differentiable rendering-based language supervision with explicit contact and penetration objectives.

3. Method

Our objective is to align two given meshes, guided by a textual description t that provides semantic context for the interaction. We refer to the two meshes as *source* and *target*; this designation is arbitrary, either mesh can play either role. The method optimizes the pose parameters $\theta = (\tau, q, s)$; translation τ , rotation q (unit quaternion), and isotropic scale s of the source mesh relative to the target until the rendered configuration agrees with t while respecting geometric and physical constraints. An overview of the pipeline is illustrated in Fig. 2.

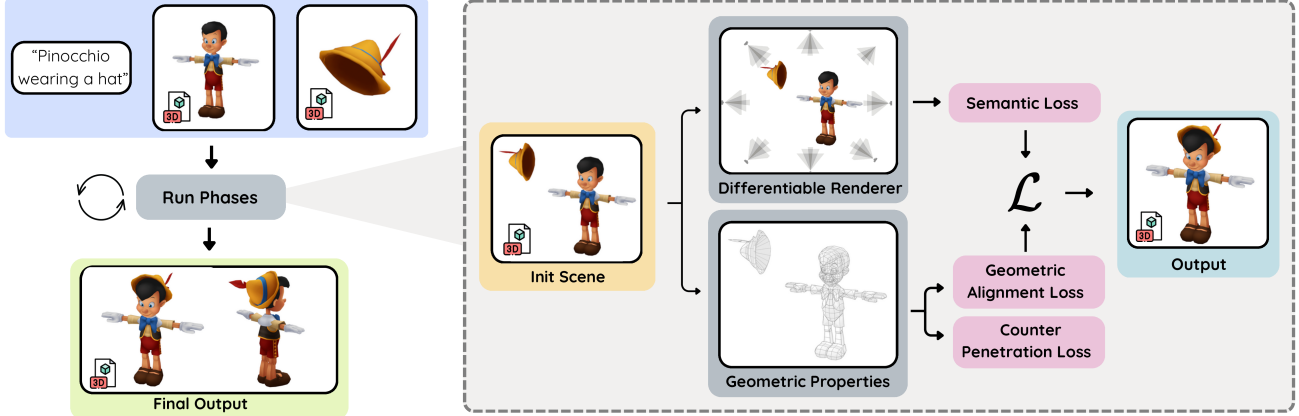


Figure 2. **Overview of the proposed pipeline.** Given two meshes and a text prompt, we optimize the relative pose and scale to produce a text-consistent alignment over P phases. In each phase, we compose the scene, render with a differentiable renderer to obtain a semantic loss, and compute geometric losses. The best result of phase i initializes phase $i+1$; across phases we increase the fractional soft-ICP and penetration weights and progressively zoom the cameras in. The final output is an aligned 3D placement of the two meshes.

3.1. Initialization

We canonicalize the target mesh with Auto-Align [2], which estimates bilateral symmetry and reorients the mesh to a common upright frame [21]. This makes the rendered views consistent with the object’s typical orientation (*e.g.*, a cup becomes upright rather than tilted), reducing view ambiguity and stabilizing semantic supervision.

3.2. Text Guidance

To guide the pose toward alignment with a textual prompt, we define a semantic objective that encourages agreement between the prompt and the rendered views in a shared image-text embedding space. We use CLIP [28] to provide this space by mapping images and text into joint embeddings. We render views with a differentiable renderer [18] \mathcal{R} , which links geometry and images and enables gradients from the similarity score to backpropagate to the 3D pose parameters.

Let M_S and M_T be the source and target meshes, respectively. At each step, we update the pose parameters θ of M_S and denote the posed mesh by \hat{M}_S . The scene is $S = M_T \cup \hat{M}_S$. We render N views $\{I_i\}_{i=1}^N$ with the differentiable renderer \mathcal{R} from cameras $\{c_i\}$ and encode each view and the prompt with CLIP, $e_i = \text{CLIP}_{\text{img}}(I_i)$ and $e_t = \text{CLIP}_{\text{text}}(t)$, and define the text-guidance loss

$$\mathcal{L}_{\text{clip}} = -\frac{1}{N} \sum_{i=1}^N \text{sim}(e_i, e_t), \quad \text{sim}(e_i, e_t) = \frac{e_i \cdot e_t}{\|e_i\| \|e_t\|}. \quad (1)$$

See Fig. 6b for a demonstration of prompt-driven controllability, where changing the text alone steers the final pose.

3.3. Geometric Objectives

Text guidance alone can yield semantically plausible but physically invalid placements. Two geometry-aware terms promote physical plausibility: (i) a fractional soft-ICP attachment term that pulls a controlled subset of source vertices toward the target vertices, and (ii) an interpenetration penalty that discourages collisions.

Fractional Soft ICP. Soft ICP replaces hard nearest-neighbor matches with probabilistic correspondences: each source vertex assigns a distribution over target vertices (*e.g.*, Gaussian weights), and the pose update minimizes the expected squared distance under these weights, improving stability under noise and partial overlap [23].

We introduce a *fractional* variant that limits attachment to only the closest subset of source vertices, controlled by a ratio $r \in (0, 1]$. Let $V_S = \{v_i^S\}_{i=1}^{N_S}$ and $V_T = \{v_j^T\}_{j=1}^{N_T}$ be the vertex sets of the source and target meshes. For each v_i^S , compute its nearest-target distance $d_i^{\min} = \min_j \|v_i^S - v_j^T\|_2$. Select the $K = \lfloor rN_S \rfloor$ indices with the smallest d_i^{\min} to form W . Define squared distances $E_{ij} = \|v_i^S - v_j^T\|_2^2$ and soft correspondences by a softmax over targets j :

$$\alpha_{ij} = \frac{\exp(-E_{ij}/(2\sigma^2))}{\sum_{j'=1}^{N_T} \exp(-E_{ij'}/(2\sigma^2))}, \quad \sum_j \alpha_{ij} = 1.$$

The attachment loss averages the expected squared distance over the selected subset:

$$\mathcal{L}_{\text{icp}}(r) = \frac{1}{K} \sum_{i \in W} \sum_{j=1}^{N_T} \alpha_{ij} E_{ij}. \quad (2)$$

Unlike standard soft-ICP, which uses all source vertices, *fractional* soft-ICP attaches only the closest r -fraction (recovering soft-ICP when $r=1$). Fig. 3 visualizes the effect

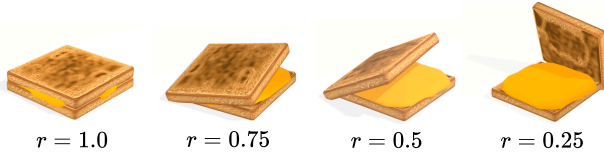


Figure 3. Effect of the alignment ratio r on a grilled-toast pair. The two objects are optimized with the same prompt, “grilled cheese toasts”, while varying r . With $r=1.0$, the top toast aligns directly above the bottom toast, producing broad surface contact; as r decreases, attachment is encouraged over a smaller subset of vertices and the contact region correspondingly shrinks.

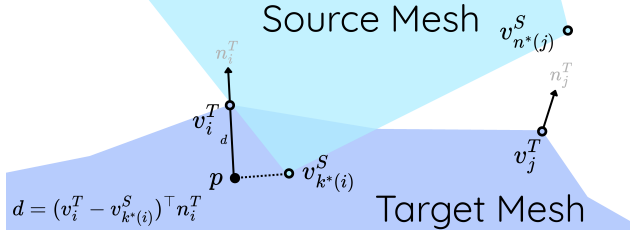


Figure 4. **Penetration loss geometry.** For target vertex v_j^T , the nearest source vertex lies outside the surface, so the signed depth and the loss term is zero. For target vertex v_i^T , the nearest source vertex is inside; the orthogonal projection onto the normal yields point p , and the signed depth $d_i > 0$ produces a positive penalty.

of the alignment ratio r : larger r enforces broader attachment across contacting surfaces, while smaller r limits attachment to a narrower region.

Penetration Loss. The penetration loss prevents invalid overlap by penalizing intrusion of the source mesh into the target mesh; a small positive margin permits limited indentation for soft materials. As in ContactOpt [13], penetration beyond a margin c_{pen} is penalized via signed depth along outward normals of the target surface. Let $\{(v_j^T, n_j^T)\}_{j=1}^{N_T}$ denote pairs of target-surface vertices and their outward normals, and let $v_{i^*(j)}^S$ be the Euclidean nearest source vertex to v_j^T :

$$\mathcal{L}_{\text{pen}} = \sum_{j=1}^{N_T} \max\left(0, (v_j^T - v_{i^*(j)}^S)^\top n_j^T - c_{\text{pen}}\right) \quad (3)$$

The margin c_{pen} governs admissible indentation: $c_{\text{pen}}=0$ for rigid contact; $c_{\text{pen}}>0$ (e.g., 2 mm) for soft materials. See Fig. 4 for an illustration.

3.4. Optimization and Scheduling

The full objective combines text guidance and geometric constraints:

$$\mathcal{L} = \lambda_{\text{CLIP}} \mathcal{L}_{\text{clip}} + \lambda_{\text{ICP}} \mathcal{L}_{\text{icp}} + \lambda_{\text{pen}} \mathcal{L}_{\text{pen}} \quad (4)$$

The Adam optimizer updates τ , q , and s of M_T . Gradients for $\mathcal{L}_{\text{clip}}$ are obtained via the differentiable renderer, while \mathcal{L}_{icp} , and \mathcal{L}_{pen} are computed directly from mesh geometry.

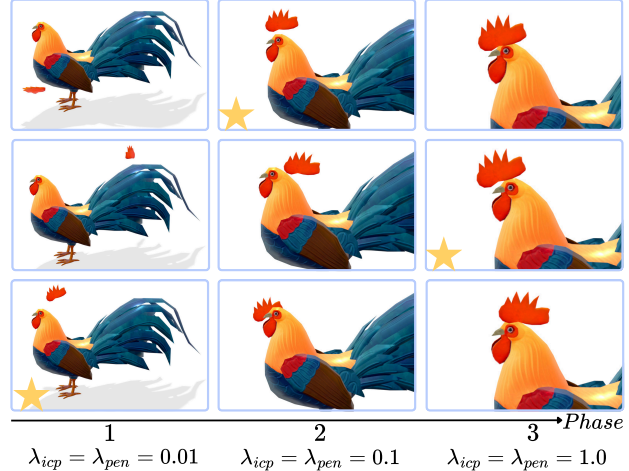


Figure 5. **Visualization of phased optimization with scheduled weights.** Rooster and comb across three phases. As the weights increase across phases, the search transitions from broad exploration to a focused zoom-in and local refinement. Phase-best results are marked with \star and initialize the next phase.

Phased optimization To balance early exploration with later contact enforcement, optimization proceeds in P successive phases. Each phase runs for a fixed number of steps; the best-scoring pose at the end of phase p initializes phase $p+1$. Two schedules are applied: (i) the fractional soft-ICP weight is increased across phases, preventing premature sticking early on and consolidating attachment later; (ii) the penetration-loss weight is similarly increased, permitting limited passage through the target mesh in early phases (e.g., inserting a flower into a vase) and progressively suppressing interpenetration afterward. Early phases emphasize exploration of candidate contact regions under language guidance with relaxed attachment and penetration; later phases focus on refinement—settling on a region, reducing interpenetration, and fine-tuning the pose. Fig. 5 visualizes this progression on a rooster-comb pair with λ_{ICP} and λ_{pen} increased by $\times 10$ between the three phases.

Camera scheduling Large scale disparities (e.g., a very small source mesh within a large target scene) can dilute gradients from language-vision scoring. Cameras are therefore scheduled across phases to progressively focus on the source mesh. Let \mathbf{c}_t be the target-mesh centroid and $\mathbf{c}_s^{(p)}$ the source-mesh centroid at phase p . The per-phase look-at target interpolates from the target to the source center,

$$\mathbf{c}^{(p)} = (1 - \beta_p) \mathbf{c}_t + \beta_p \mathbf{c}_s^{(p)}, \quad 0 = \beta_1 < \dots < \beta_P \leq 1.$$

Simultaneously, the camera distance is reduced to zoom in while keeping coverage. Early phases thus provide global context; later phases concentrate on the source mesh to expose finer details to the vision-language guidance. See Fig. 5 for an example of this zoom-in and look-at progression across phases.

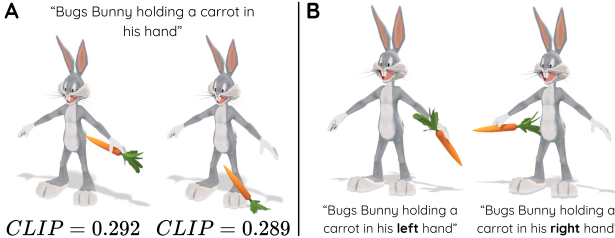


Figure 6. **Initialization variability and prompt controllability.** (a) Two random initializations of the carrot w.r.t. Bugs Bunny converge to distinct yet plausible attachments; we run several restarts and pick the best by a CLIP text–image score (higher is better). (b) With the same meshes, two prompts steer optimization to different, prompt-consistent placements, demonstrating language controllability.

3.5. Random restarts and per-step noise

Pose optimization is local and sensitive to initialization: if the source mesh starts near an unintended region of the target mesh, the optimizer can converge to a spurious contact. To mitigate this, the procedure launch N independent initializations and runs the same objective for a fixed number of optimization steps. The final estimate is chosen by the highest evaluation score. Fig. 6a illustrates the impact of initialization. Starting from two different random placements of the carrot relative to Bugs Bunny, the optimization converges to distinct yet plausible attachment points. This sensitivity motivates running multiple restarts and selecting the best result under the objective.

In addition, a small zero-mean perturbation is added to the pose parameters at each iteration. This stochastic jitter encourages exploration and helps escape local minima.

3.6. LLM-guided hyperparameter selection

At test time, we query a large language model (LLM) with the prompt t and the two object names to obtain scene priors that set a few method hyperparameters.

Penetration policy. The LLM returns a boolean indicating whether the final arrangement should involve penetration (e.g., “*knife cuts an apple*” \Rightarrow allow penetration). If penetration is allowed, we set the penetration term weight to zero during optimization; otherwise we use the default penetration schedule.

Initial scale. The LLM estimates the real-world size ratio between the source and target objects. We clamp the returned value to $[0.1, 10]$ and use it to initialize the scale.

Attachment ratio. For fractional soft-ICP, the LLM provides a coarse assessment of contact extent between the objects, which we map to the attachment ratio $r \in [0, 1]$ controlling the fraction of vertices selected for attachment.

4. Experiments

4.1. Experimental Setup

Benchmark. Evaluation is conducted on a diverse set of 50 mesh pairs and text prompts covering a range of object–object relations, such as “*A sundae with a cherry on top*”, “*A candle sits inside a candle holder*” and “*Pinocchio wearing a hat*”. The benchmark, including meshes and prompts, will be released upon publication.

Computation and schedule. We run 2,000 optimization steps per pair with a batch of 8 camera views per step. Optimization proceeds in $P=3$ phases; across phases, the fractional soft-ICP and penetration weights follow a logarithmic increase, encouraging broad exploration early and stronger contact enforcement later. Camera scheduling (progressive zoom-in and look-at interpolation) follows Sec. 3.4.

Initialization and Preprocessing. For meshes with low or uneven vertex density, we apply remeshing to ensure sufficient sampling for vertex-based geometric losses and to avoid degenerate boundary-only surfaces. To mitigate local minima, each experiment uses multiple randomized initial poses of the source mesh (see Sec. 3.5). We run $N = 5$ restarts under the same settings and automatically select the best-scoring pose by the total objective value.

4.2. Metrics

OOA must satisfy both semantic intent and physical plausibility. We therefore report complementary semantic and geometric metrics.

Semantic metrics. We render the final alignment from $N=8$ fixed evaluation cameras and average image-text agreement across views using three vision-language encoders: CLIP [28], ALIGN [15], and SigLIP [35]. Higher values indicate stronger text alignment.

Intersection. Physical plausibility is assessed by volumetric overlap between the meshes. We report the *intersection ratio*

$$\text{Inter.} = \frac{\text{Vol}(\text{mesh}_1 \cap \text{mesh}_2)}{\text{Vol}(\text{mesh}_1 \cup \text{mesh}_2)} \in [0, 1].$$

Lower values correspond to fewer inter-penetrations.

VLM evaluator. We additionally report GPT-4V-based automatic scores following GPTEval3D [37], covering four criteria: Text-Asset Alignment, 3D Plausibility, Text-Geometry Alignment, and Overall. We omit the GPTEval3D Texture Details and Geometry Details criteria because all methods operate on the same input meshes; thus, texture and base geometry are shared (up to minor differences induced by the optimization), making these scores uninformative for method comparison.

4.3. Baselines

Language-guided OOA is a relatively new problem, thus methods with exactly the same objective are scarce. Accordingly, we evaluate against one method that pursues the same goal as ours, two closely related LLM-based methods, and two geometry-based methods.

Object-object spatial relationships (OOR) diffusion [3]. This method proceeds in two stages: (i) it creates training data by sampling a pretrained 2D diffusion model to synthesize diverse object-pair images and uplifting them to 3D to obtain relative pose/scale examples; (ii) it trains a text-conditioned score-based diffusion over the spatial parameter space and samples configurations at test time. As no implementation or checkpoints are available, we include this baseline only in the qualitative comparison (Sec. 4.6).

SceneMotifCoder (SMC) [34]. SMC learns meta-programs for 3D arrangements from a few examples; at inference it uses an LLM to instantiate program arguments, retrieves meshes, and runs a geometry-aware optimization to produce physically plausible placements.

SceneTeller [24]. SceneTeller is an LLM-driven scene arrangement method. Although designed for indoor scene layouts, its language-to-layout interface allows us to pose two-object cases as minimal “scenes”, enabling a comparison on OOA scenarios.

(B1) Shrinkwrap (single start). The source mesh is projected onto the target mesh using a shrinkwrap constraint [6], which attaches vertices to the nearest points on the target surface. This baseline is geometry-only and uses no text guidance.

(B2) Shrinkwrap (multi-start + CLIP selection). The shrinkwrap procedure is repeated with $N = 5$ randomized initial poses. Each resulting placement is scored using the CLIP similarity metric, and the best-scoring pose is selected. This variant retains a geometric projection step but incorporates semantic selection via CLIP, yielding a stronger baseline than B1.

4.4. Quantitative Results

Tab. 1 summarizes averages across the benchmark using the metrics in Sec. 4.2. Our method attains the highest semantic scores on all three measures while maintaining competitive intersection volume. Notably, across the baselines, SceneTeller achieves the lowest intersection on average, but this often coincides with weaker semantic alignment, see the qualitative comparisons in Fig. 9, where placements that minimize penetration can still miss the intended interaction. As a trade-off summary, Fig. 7 plots CLIP and ALIGN versus intersection volume; in all panels our method lies bottom-right, indicating the best combination of high semantic agreement and low interpenetration. On the VLM-based evaluator, our method also ranks first among the baselines on all reported criteria: Text-Asset Alignment, 3D



Figure 7. **Trade-off plot.** CLIP, ALIGN score vs. intersection volume score. Down and to the right is better. The full visualization, including SigLIP, is provided in the supplementary.



Figure 8. **Ablations on coatrack (target) and hat (source).** The full method yields the most plausible, text-aligned placement; ablating individual components produces degradations.

Plausibility, Text-Geometry Alignment, and Overall. We additionally report a scale-enabled variant, which is listed separately because competing baselines operate in a rigid setting and do not optimize scale.

4.5. Ablation Study

We evaluate *w/o guidance* (no semantic text guidance), *w/o soft-ICP*, *w/o penetration*, *w/o phases*, *w/o camera adjustment*, *SDS* (replace CLIP with score distillation sampling [26]), and *SigLIP-guidance* (replace CLIP with SigLIP). Quantitative comparison appear in Tab. 2. The *w/o camera adjustment* variant appears close on averages because its benefit is most pronounced for large size-ratio pairs which is a minority of the benchmark. We hypothesize SDS underperforms in this setting because its stochastic, synthesis-oriented gradients provide weaker directional signals for pose updates compared to CLIP’s contrastive image-text similarity. Fig. 8 illustrates these effects on a *coatrack & hat* example: the full model yields the most physically plausible, text-aligned placement, while ablations exhibit the characteristic failures described above.

4.6. Qualitative Results

Fig. 9 compares our method with *B1*, *B2*, *SceneTeller*, and *SMC*. Our method consistently produces semantically faithful, physically plausible placements. *B1*, *SceneTeller* and *SMC* often misplace the source on irrelevant regions or exhibit interpenetrations, while *B2* improves semantic consistency but still shows physical or semantic mismatches.

We also include a side-by-side with *OOR-diffusion*

Method	CLIP \uparrow	ALIGN \uparrow	SigLIP \uparrow	Intersection Volume \downarrow	Text-Asset Alignment \uparrow	3D Plausibility \uparrow	Text-Geometry Alignment \uparrow	Overall \uparrow
Ours	0.3224	14.9800	0.0380	0.0112	1028.72	1024.06	1068.47	1034.44
B1	0.3087	14.1484	0.0374	0.0090	988.63	1022.38	960.55	1005.92
B2	0.3157	14.1897	0.0362	0.0118	997.41	987.63	980.59	1019.69
SceneTeller	0.3040	13.2522	0.0367	0.0051	986.40	989.41	938.30	963.80
SMC	0.3069	14.1704	0.0370	0.0244	985.75	991.30	937.56	991.19
Ours (+ scale)	0.3176	15.0350	0.0380	0.0110	994.52	959.33	1029.71	1005.10

Table 1. **Baseline comparison.** Semantic alignment (CLIP/ALIGN/SigLIP; higher is better), physical plausibility (intersection volume; lower is better), and VLM evaluator scores (Text-Asset, 3D Plausibility, Text-Geometry, Overall; higher is better).

Method	CLIP \uparrow	ALIGN \uparrow	SigLIP \uparrow	Intersection Volume \downarrow	Text-Asset Alignment \uparrow	3D Plausibility \uparrow	Text-Geometry Alignment \uparrow	Overall \uparrow
Ours	0.3224	14.9800	0.0380	0.0112	1028.72	1024.06	1068.47	1034.44
w/o guidance	0.3091	13.8372	0.0372	0.0099	985.52	979.31	959.38	999.79
w/o soft-ICP	0.3214	14.7183	0.0368	0.0002	969.40	1031.15	976.74	1004.89
w/o penet.	0.3223	14.7342	0.0376	0.0177	1007.71	1000.49	961.71	987.69
w/o phases	0.3214	14.7627	0.0379	0.0141	978.24	965.52	974.38	996.56
w/o camera adj.	0.3201	14.5859	0.0368	0.0127	1035.74	1019.02	1004.62	1023.30
SDS	0.3167	14.4120	0.0377	0.0148	1022.78	1002.96	1010.46	1005.47
SigLIP	0.3145	14.4185	0.0387	0.0136	1015.86	1014.75	1019.08	1025.52

Table 2. **Ablation comparison.** Ablated variants across semantic alignment (CLIP/ALIGN/SigLIP; higher is better), physical plausibility (intersection volume; lower is better), and VLM evaluator scores (Text-Asset, 3D Plausibility, Text-Geometry, Overall; higher is better).

Question	Ours	B1	B2	SceneTeller	SMC
Matches description (%)	85.24	3.32	7.98	1.73	1.73
Physically plausible (%)	79.65	3.86	8.78	1.99	5.72

Table 3. **User study results.** Percentage of votes across 15 instances and 47 participants. Higher is better.

(Fig. 10). As no implementation or checkpoints are available, we extracted *OOR-diffusion* images from their paper and qualitatively compare on those highlighted examples. For these cases, both methods produce text-aligned and physically plausible results. Where possible, we reproduced our results with similar assets and camera poses, though exact assets/cameras may differ.

4.7. User study

We conducted a user study comparing our method to four baselines (B1, B2, SceneTeller, SMC) on 15 object-pair instances, randomly selected from our benchmark, with 47 participants. In each trial, participants were shown (i) the names of the two objects, (ii) the text prompt describing their interaction, and (iii) five rendered images, one per method, presented together. For every trial they answered two multiple-choice questions: (1) *Which image best matches the textual description of the interaction?* and (2) *In which image the two objects appear most physically plausible?* Method order and trial order were randomized per participant. Results appear in Tab. 3. Full protocol details appear in the Supplementary.

4.8. Evaluation of LLM hyperparameter selection

We evaluate the LLM on a held-out set of 61 object-pair instances with ground-truth (GT) labels equal to the hyperparameters defined in Sec. 3.6: (i) initial scale ratio, (ii)

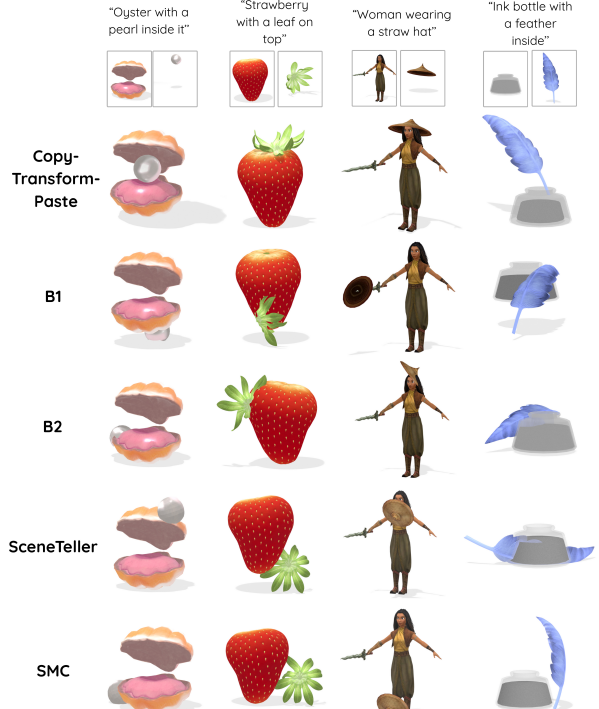


Figure 9. **Qualitative comparison across four object-object pairs.** Top row: input prompt and meshes. Rows 1–5: final placements from our method and baselines. Our approach yields semantically faithful and physically plausible alignments, while baselines vary in semantic faithfulness and contact quality.

penetration policy, and (iii) attachment ratio. For each instance, the LLM receives only the two object names and the text prompt and returns one value per hyperparameter. We repeated 10 independent queries per instance. We report accuracy for the binary penetration label, and Mean Absolute



Figure 10. **Qualitative comparison to OOR-diffusion.** OOR-diffusion panels are reproduced from their paper; we matched assets and camera setups where possible.

	Penet. (Acc. % \uparrow) boolean	Init. scale (MAE \downarrow) [0.1, 10]	Attach. ratio (MAE \downarrow) [0, 1]
LLM (ours)	98.36	0.46	0.25
Random	50.00	3.30	0.33

Table 4. **LLM hyperparameter selection.** Results on 61 held-out object-pair instances. The LLM predicts three hyperparameters: penetration policy, initial scale ratio, and attachment ratio. The random baseline corresponds to expectations from uniform sampling over the indicated ranges.



Figure 11. **Image-to-3D alignment.** Inputs: image + two meshes. Output: aligned meshes whose renders match the image.

Error (MAE) for the continuous quantities: initial scale and attachment ratio (Tab. 4).

5. Other applications

Image-to-3D alignment. Given an image and two meshes, we render candidate views and use the same language-vision objectives to align the meshes so that the rendered views agree with the image description (see Fig. 11).

Multi-object assembly (iterative). We can align multiple objects by iterating: the output of stage k becomes part of the input at stage $k+1$, progressively assembling the scene (see Fig. 1, bottom-right).



Figure 12. **Failure cases.** Errors from multi-view ambiguity and insertion into cavity, extreme scale mismatch that weakens language guidance, and residual interpenetration (often mitigated by re-running or increasing the penetration weight).

6. Limitations

While the proposed method demonstrates robust and semantically coherent object-object alignment, several limitations remain.

Penetration residuals. Despite the penetration loss, the final placements may exhibit minor interpenetrations. Increasing the penetration weight in later phases or re-running with different random initializations often mitigates this.

View scheduling and finite-view supervision. Because cameras are re-targeted across phases (Sec. 3.4) and gradients are computed from a finite set of views, viewpoint-sensitive predicates such as “*beside/next to/left of/right of*” can be unstable: the lateral frame of reference shifts with the current view, and solutions that look correct from the sampled angles may still be wrong in 3D.

Extreme scale differences and partial visibility. When objects differ greatly in size, the smaller one may occupy a negligible fraction of the image, yielding unreliable language-vision gradients even with zoom-in scheduling. Similar degradation appears under heavy occlusion (e.g., insertion into a cavity). These effects align with reported CLIP biases toward the more salient or larger object in multi-object scenes [1].

Fig. 12 illustrates representative cases for viewpoint sensitivity, extreme scale, and penetration residuals.

7. Conclusion

This work introduced a text-guided framework for aligning two 3D meshes under vision-language supervision and geometric constraints. By optimizing translation, rotation, and scale through differentiable rendering, the method achieves semantically faithful and physically plausible arrangements. A benchmark of text-mesh-mesh triplets enables standardized evaluation of text-guided object alignment. Extensive experiments demonstrate robustness and highlight the roles of geometric and language-based objectives. Future work will explore stronger vision-language models, multi-view consistency, and physics-based reasoning to further improve realism.

References

[1] Reza Abbasi, Ali Nazari, Aminreza Sefid, Mohammadi Banayeeanzade, Mohammad Hossein Rohban, and Mahdieh Soleymani Baghshah. Clip under the microscope: A fine-grained analysis of multi-object representation. In *Proceedings of the IEEE/CVF Conference on Computer Vision and Pattern Recognition (CVPR)*, pages 9308–9317, 2025. 8

[2] Auto-Align contributors. Auto-align. <https://github.com/cube-c/Auto-Align>, 2023. Accessed 2025-09-04. 3

[3] Sangwon Baik, Hyeonwoo Kim, and Hanbyul Joo. Learning 3d object spatial relationships from pre-trained 2d diffusion models. *arXiv preprint arXiv:2503.19914*, 2025. 6

[4] Paul J Besl and Neil D McKay. Method for registration of 3-d shapes. In *Sensor fusion IV: control paradigms and data structures*, pages 586–606. Spie, 1992. 2

[5] Bharat Lal Bhatnagar, Xianghui Xie, Ilya A Petrov, Cristian Sminchisescu, Christian Theobalt, and Gerard Pons-Moll. Behave: Dataset and method for tracking human object interactions. In *Proceedings of the IEEE/CVF Conference on Computer Vision and Pattern Recognition*, pages 15935–15946, 2022. 1

[6] Blender Online Community. Blender manual: Shrinkwrap constraint. <https://docs.blender.org/manual/en/latest/animation/constraints/relationship/shrinkwrap.html>, 2025. Accessed: 2025-09-29. 6

[7] Yang Chen and Gérard Medioni. Object modelling by registration of multiple range images. *Image and vision computing*, 10(3):145–155, 1992. 2

[8] Yun-Chun Chen, Selena Ling, Zhiqin Chen, Vladimir G Kim, Matheus Gadelha, and Alec Jacobson. Text-guided controllable mesh refinement for interactive 3d modeling. In *SIGGRAPH Asia 2024 Conference Papers*, pages 1–11, 2024. 2

[9] Ziya Erkoç, Can Gümeli, Chaoyang Wang, Matthias Nießner, Angela Dai, Peter Wonka, Hsin-Ying Lee, and Peiye Zhuang. Predictor3d: Fast and precise 3d shape editing. In *Proceedings of the Computer Vision and Pattern Recognition Conference*, pages 640–649, 2025. 2

[10] Kevin Frans, Lisa Soros, and Olaf Witkowski. Clipdraw: Exploring text-to-drawing synthesis through language-image encoders. *Advances in Neural Information Processing Systems*, 35:5207–5218, 2022. 2

[11] Rinon Gal, Or Patashnik, Haggai Maron, Amit H Bermano, Gal Chechik, and Daniel Cohen-Or. Stylegan-nada: Clip-guided domain adaptation of image generators. *ACM Transactions on Graphics (TOG)*, 41(4):1–13, 2022. 2

[12] William Gao, Noam Aigerman, Thibault Groueix, Vova Kim, and Rana Hanocka. Textdeformer: Geometry manipulation using text guidance. In *ACM SIGGRAPH 2023 conference proceedings*, pages 1–11, 2023. 2

[13] Patrick Grady, Chengcheng Tang, Christopher D Twigg, Minh Vo, Samarth Brahmbhatt, and Charles C Kemp. Contactopt: Optimizing contact to improve grasps. In *Proceedings of the IEEE/CVF Conference on Computer Vision and Pattern Recognition*, pages 1471–1481, 2021. 4

[14] Ajay Jain, Ben Mildenhall, Jonathan T Barron, Pieter Abbeel, and Ben Poole. Zero-shot text-guided object generation with dream fields. In *Proceedings of the IEEE/CVF conference on computer vision and pattern recognition*, pages 867–876, 2022. 2

[15] Chao Jia, Yinfai Yang, Ye Xia, Yi-Ting Chen, Zarana Parekh, Hieu Pham, Quoc Le, Yun-Hsuan Sung, Zhen Li, and Tom Duerig. Scaling up visual and vision-language representation learning with noisy text supervision. In *International conference on machine learning*, pages 4904–4916. PMLR, 2021. 5

[16] Hiroharu Kato, Yoshitaka Ushiku, and Tatsuya Harada. Neural 3d mesh renderer. In *Proceedings of the IEEE conference on computer vision and pattern recognition*, pages 3907–3916, 2018. 1, 2

[17] Gwanghyun Kim, Taesung Kwon, and Jong Chul Ye. Diffusionclip: Text-guided diffusion models for robust image manipulation. In *Proceedings of the IEEE/CVF conference on computer vision and pattern recognition*, pages 2426–2435, 2022. 2

[18] Samuli Laine, Janne Hellsten, Tero Karras, Yeongho Seol, Jaakko Lehtinen, and Timo Aila. Modular primitives for high-performance differentiable rendering. *ACM Transactions on Graphics (ToG)*, 39(6):1–14, 2020. 1, 2, 3

[19] Shichen Liu, Tianye Li, Weikai Chen, and Hao Li. Soft rasterizer: A differentiable renderer for image-based 3d reasoning. In *Proceedings of the IEEE/CVF international conference on computer vision*, pages 7708–7717, 2019. 1, 2

[20] Oscar Michel, Roi Bar-On, Richard Liu, Sagie Benaim, and Rana Hanocka. Text2mesh: Text-driven neural stylization for meshes. In *Proceedings of the IEEE/CVF conference on computer vision and pattern recognition*, pages 13492–13502, 2022. 2

[21] Niloy J Mitra, Mark Pauly, Michael Wand, and Duygu Ceylan. Symmetry in 3d geometry: Extraction and applications. In *Computer graphics forum*, pages 1–23. Wiley Online Library, 2013. 3

[22] Nasir Mohammad Khalid, Tianhao Xie, Eugene Belilovsky, and Tiberiu Popa. Clip-mesh: Generating textured meshes from text using pretrained image-text models. In *SIGGRAPH Asia 2022 conference papers*, pages 1–8, 2022. 2

[23] Andriy Myronenko and Xubo Song. Point set registration: Coherent point drift. *IEEE transactions on pattern analysis and machine intelligence*, 32(12):2262–2275, 2010. 2, 3

[24] Başak Melis Öcal, Maxim Tatarchenko, Sezer Karaoglu, and Theo Gevers. Sceneteller: Language-to-3d scene generation. In *European Conference on Computer Vision*, pages 362–378. Springer, 2024. 6

[25] Or Patashnik, Zongze Wu, Eli Shechtman, Daniel Cohen-Or, and Dani Lischinski. Styleclip: Text-driven manipulation of stylegan imagery. In *Proceedings of the IEEE/CVF international conference on computer vision*, pages 2085–2094, 2021. 2

[26] Ben Poole, Ajay Jain, Jonathan T Barron, and Ben Mildenhall. Dreamfusion: Text-to-3d using 2d diffusion. *arXiv preprint arXiv:2209.14988*, 2022. 2, 6

[27] Yu Qi, Yuanchen Ju, Tianming Wei, Chi Chu, Lawson LS Wong, and Huazhe Xu. Two by two: Learning multi-task pairwise objects assembly for generalizable robot manipulation. In *Proceedings of the Computer Vision and Pattern Recognition Conference*, pages 17383–17393, 2025. 1

[28] Alec Radford, Jong Wook Kim, Chris Hallacy, Aditya Ramesh, Gabriel Goh, Sandhini Agarwal, Girish Sastry, Amanda Askell, Pamela Mishkin, Jack Clark, et al. Learning transferable visual models from natural language supervision. In *International conference on machine learning*, pages 8748–8763. PMLR, 2021. 2, 3, 5

[29] Szymon Rusinkiewicz and Marc Levoy. Efficient variants of the icp algorithm. *Proceedings Third International Conference on 3-D Digital Imaging and Modeling*, pages 145–152, 2001. 2

[30] Andrei Sharf, Marina Blumenkrants, Ariel Shamir, and Daniel Cohen-Or. Snappaste: an interactive technique for easy mesh composition. *The Visual Computer*, 22(9):835–844, 2006. 2

[31] Yiren Song, Xuning Shao, Kang Chen, Weidong Zhang, Zhongliang Jing, and Minzhe Li. Clipvg: Text-guided image manipulation using differentiable vector graphics. In *Proceedings of the AAAI conference on artificial intelligence*, pages 2312–2320, 2023. 2

[32] Omid Taheri, Nima Ghorbani, Michael J Black, and Dimitrios Tzionas. Grab: A dataset of whole-body human grasping of objects. In *European conference on computer vision*, pages 581–600. Springer, 2020. 1

[33] Gary KL Tam, Zhi-Quan Cheng, Yu-Kun Lai, Frank C Langbein, Yonghuai Liu, David Marshall, Ralph R Martin, Xian-Fang Sun, and Paul L Rosin. Registration of 3d point clouds and meshes: A survey from rigid to nonrigid. *IEEE transactions on visualization and computer graphics*, 19(7):1199–1217, 2012. 2

[34] Hou In Ivan Tam, Hou In Derek Pun, Austin T. Wang, Angel X. Chang, and Manolis Savva. SceneMotifCoder: Example-driven Visual Program Learning for Generating 3D Object Arrangements. In *Proceedings of the IEEE Conference on 3D Vision (3DV)*, 2025. 6

[35] Michael Tschanne, Alexey Gritsenko, Xiao Wang, Muhammad Ferjad Naeem, Ibrahim Alabdulmohsin, Nikhil Parthasarathy, Talfan Evans, Lucas Beyer, Ye Xia, Basil Mustafa, et al. Siglip 2: Multilingual vision-language encoders with improved semantic understanding, localization, and dense features. *arXiv preprint arXiv:2502.14786*, 2025. 5

[36] Yael Vinker, Ehsan Pajouheshgar, Jessica Y Bo, Roman Christian Bachmann, Amit Haim Bermano, Daniel Cohen-Or, Amir Zamir, and Ariel Shamir. Clipasso: Semantically-aware object sketching. *ACM Transactions on Graphics (TOG)*, 41(4):1–11, 2022. 2

[37] Tong Wu, Guandao Yang, Zhibing Li, Kai Zhang, Ziwei Liu, Leonidas Guibas, Dahua Lin, and Gordon Wetzstein. Gpt-4v (ision) is a human-aligned evaluator for text-to-3d generation. In *Proceedings of the IEEE/CVF conference on computer vision and pattern recognition*, pages 22227–22238, 2024. 5

COPY-TRANSFORM-PASTE: Zero-Shot Object-Object Alignment Guided by Vision-Language and Geometric Constraints

Supplementary Material

8. Benchmark Construction

Two curated benchmarks. We release two OOA variants: (i) **Rigid** (translation+rotation only; no scale) and (ii) **Scale-enabled** (translation+rotation+isotropic scale). This separation enables fair comparison to methods that do not support scale.

Source assets and reference pose. We collected pairs of meshes from Sketchfab. For each pair, we manually placed the objects in their intended relational configuration (e.g., candle inside candlestick). This serves as the reference pose. It fixes only the relative arrangement; meshes are not necessarily canonicalized or upright.

Perturbation protocol (initializations). Starting from the reference pose, we create randomized starting positions by selecting one object at random and:

- **Translate** each mesh independently by a random offset $\Delta \sim \mathcal{U}(-10\mathbf{L}, 10\mathbf{L})$, where $\mathbf{L} = (L_x, L_y, L_z)$ are the side lengths of its axis-aligned bounding box.
- **Rotate** it by independent Euler angles within $\pm 180^\circ$.
- **Scale** (for the *scale-enabled* benchmark only) isotropically, sampled uniformly from $[0.01, 100.0]$.

All draws are uniform and independent; the *rigid* benchmark keeps the scale fixed at 1.0.

Outputs. For each benchmark instance we also provide: (1) the *final aligned meshes*, and (2) the *text prompt*.

9. LLM prompt design for hyperparameter selection

In Sec. 3.6, we described how an LLM is used to estimate three hyperparameters from the object names and scene description. Here, we provide the exact prompts used to query the model. Each prompt is written in natural language and instructs the model to output a single JSON value on one line.

(1) Initial scale. Estimates the real-world relative size between the two objects: Estimate the relative scale needed so that $\text{object1}=\{\text{object1}\}$ and $\text{object2}=\{\text{object2}\}$ fit together naturally in the desired alignment "`{wanted_alignment}`".

Define `size_ratio = bbox_size(object1) / bbox_size(object2)`. Output exactly one JSON

```
object: {"size_ratio": <float between 0.01 and 100.0>}.
```

(2) Penetration policy. Determines whether the final configuration should involve one object penetrating another (e.g., cutting, slicing): Decide whether achieving alignment "`{wanted_alignment}`" between $\text{object1}=\{\text{object1}\}$ and $\text{object2}=\{\text{object2}\}$ REQUIRES solid-to-solid penetration. Output exactly one JSON object: `{"penetration": <true|false>}`.

(3) Attachment ratio. Estimates how much surface contact is expected between the two objects in the final arrangement: For the desired alignment "`{wanted_alignment}`", estimate the fraction of surface contact between $\text{object1}=\{\text{object1}\}$ and $\text{object2}=\{\text{object2}\}$ ". Define `contact_ratio` in $[0, 1]$, where 0 = almost no contact and 1 = full surface contact. Output exactly one JSON object: `{"contact_ratio": <float 0..1>}`.

Usage. At test time, we query the LLM with these three templates using only the object names and textual prompt, without any rendered images. The model outputs the three values used to set: (i) the source-object initial scale, (ii) whether the penetration loss is enabled, and (iii) the attachment ratio r controlling the soft-ICP vertex fraction.

10. User Study Protocol

We include here the full user study protocol used in our evaluation, consisting of the instructions shown to participants (Fig. 14) and an example trial interface (Fig. 15). These materials were presented exactly as shown to all participants during the study.

11. Additional Trade-off Visualizations

Figure 13 provides the full trade-off visualization referenced in the main paper, including results for SigLIP in addition to CLIP and ALIGN.

12. Additional Image-to-3D Alignment Results

Beyond text-conditioned alignment, our method can also be guided by reference images. Figure 16 presents additional examples of this image-to-3D setting. Each row shows the two input meshes, the guiding reference image, and the final optimized arrangement.

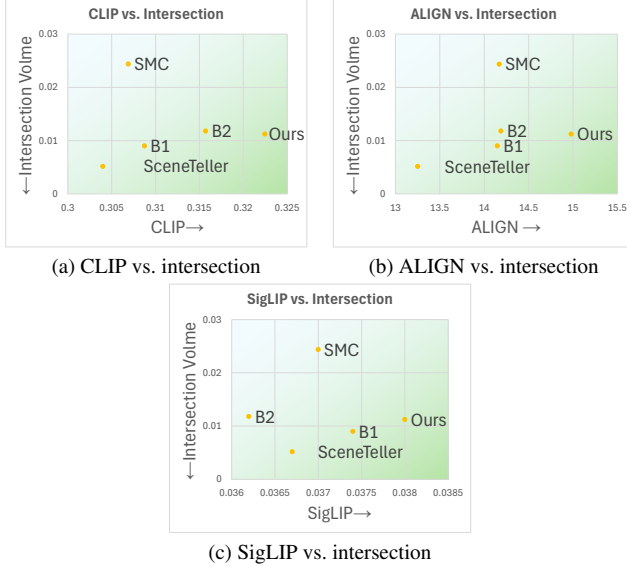


Figure 13. **Extended trade-off plots.** Vision–language alignment score versus intersection volume. Lower intersection and higher alignment (down-right) is better.

13. Additional Qualitative Comparisons

We include additional per-mesh qualitative comparisons between our method and the four baselines (B1, B2, SceneTeller, and SMC). For each prompt, the figures show (left to right) the target mesh alone followed by the final aligned meshes rendered from four different viewpoints. These supplementary examples cover a diverse set of physical and semantic relationships and illustrate consistent improvements of our method across cases. See Figs. 17 to 24 for the full set of comparisons.

User Study: Evaluating Object-Object Interactions

x

:

In this study, you will be presented with **15 short text descriptions** (for example, "A hot dog sausage sits inside a bun").

For each description, you will see **five rendered images** (A-E), each created by a different method.

Each section includes **pair of objects, text description, and five images**.

You will answer **two questions per description** about the images and the given pair.

1. **Matches the description** - Which image best represents the interaction **between the two objects**, in a natural and expected way (both objects are present and arranged as described)?
2. **Looks physically correct** - In which image the **two objects** appear most physically plausible (the two objects are placed naturally, no floating, and no part of one object passes through the other)?

Please base your answers **only** on these criteria and **ignore** lighting, color, or texture differences.

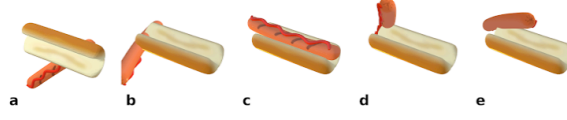
We recommend using a **computer or laptop** (not a phone) so the images are larger and differences are clearer.

The study should take about **5-7 minutes** to complete.

Figure 14. User study guidelines (screenshot).

0. Example Question

Hotdog - Bun *
 Prompt: 'A **hot dog** sausage sits inside a **bun**.'



Which image best represents the interaction between the two objects?

a b c d e

In which image the two objects appear most physically plausible?

a b c d e

Figure 15. Example trial (screenshot).

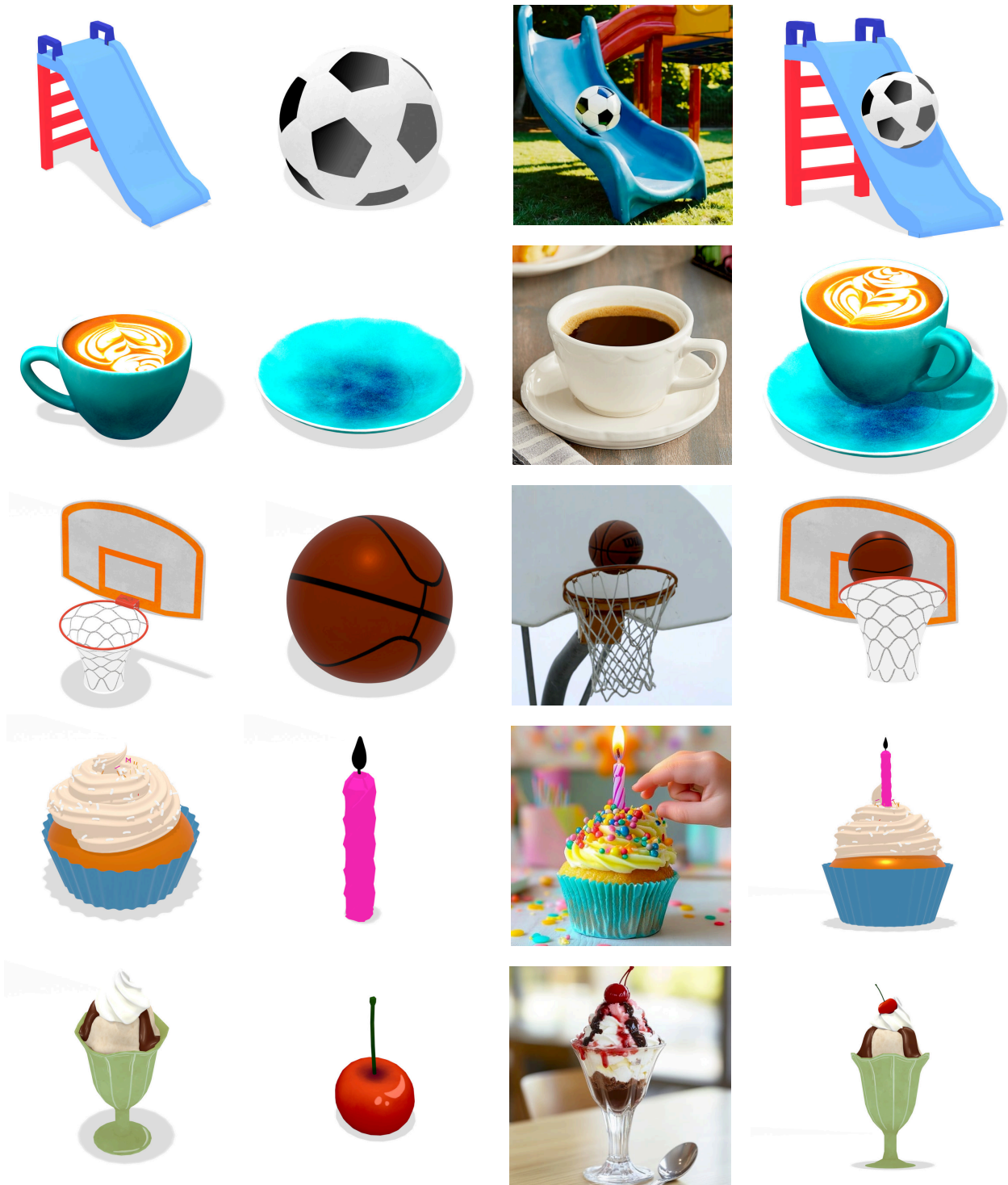


Figure 16. **Additional image-to-3D alignment results.** Each row shows an example of our image-guided alignment process: the two input meshes (left), the reference image used for guidance (middle), and the final optimized placement (right). These examples illustrate the model’s ability to interpret image cues and produce semantically consistent 3D arrangements.

“Ice cream sits inside a cone”

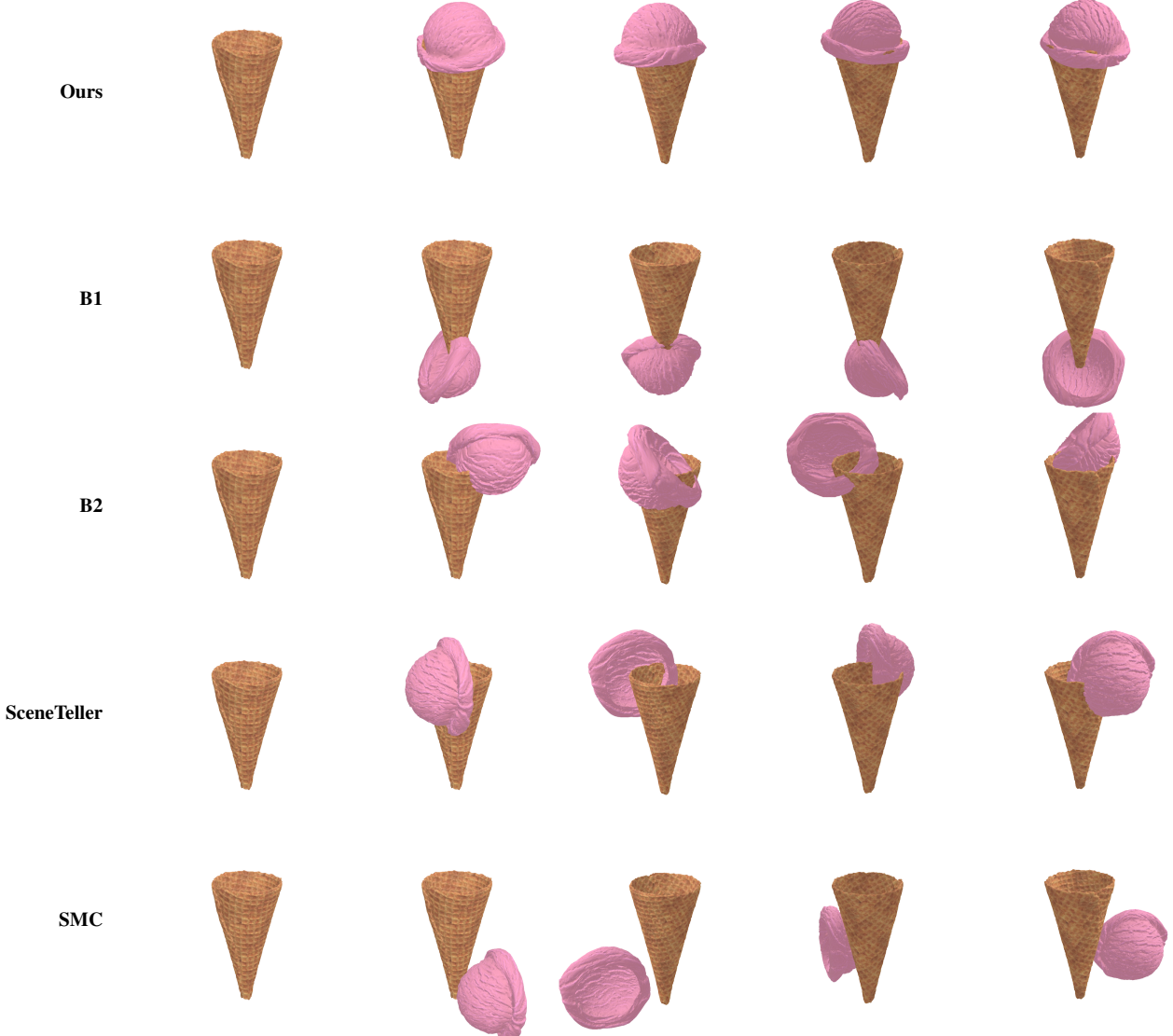


Figure 17. **Per-mesh qualitative comparison: ice cream and cone.** Rows correspond to our method, B1, B2, SceneTeller, and SMC (top to bottom). In each row, the leftmost panel shows the target mesh alone, followed by the final aligned meshes rendered from four different viewing angles. Only our method achieves a text-aligned configuration where the ice cream sits physically inside the cone.

“A blender jar sits on top of the blender base”

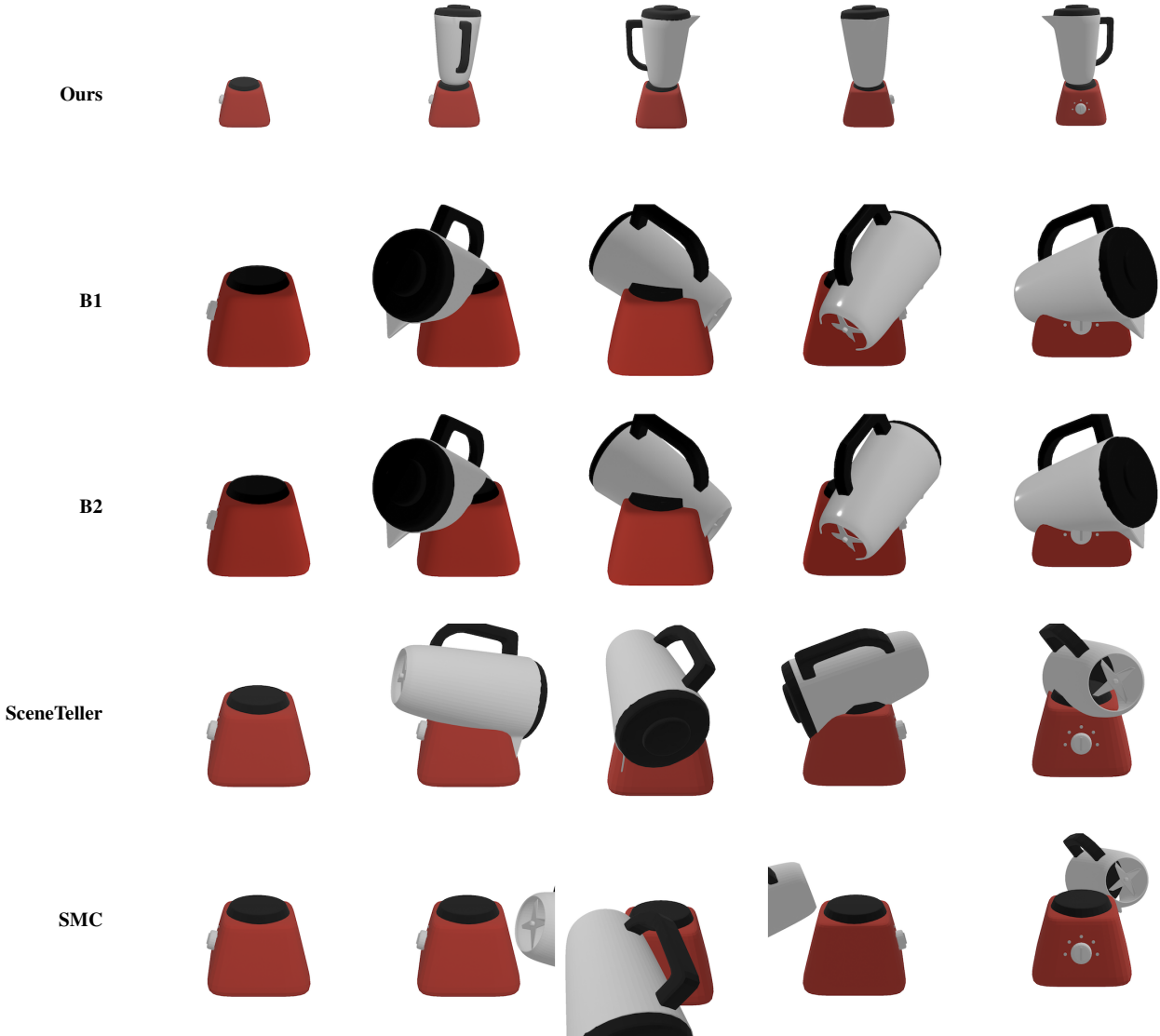


Figure 18. **Per-mesh qualitative comparison: blender jar and base.** Rows correspond to our method, B1, B2, SceneTeller, and SMC (top to bottom). In each row, the leftmost panel shows the target mesh alone, followed by the final aligned meshes rendered from four different viewing angles. Only our method places the jar upright and stably on the base; other baselines do put the jar on top but typically tilt it and exhibit noticeable interpenetrations between jar and base.

“Hot dog sausage sits inside a bun”

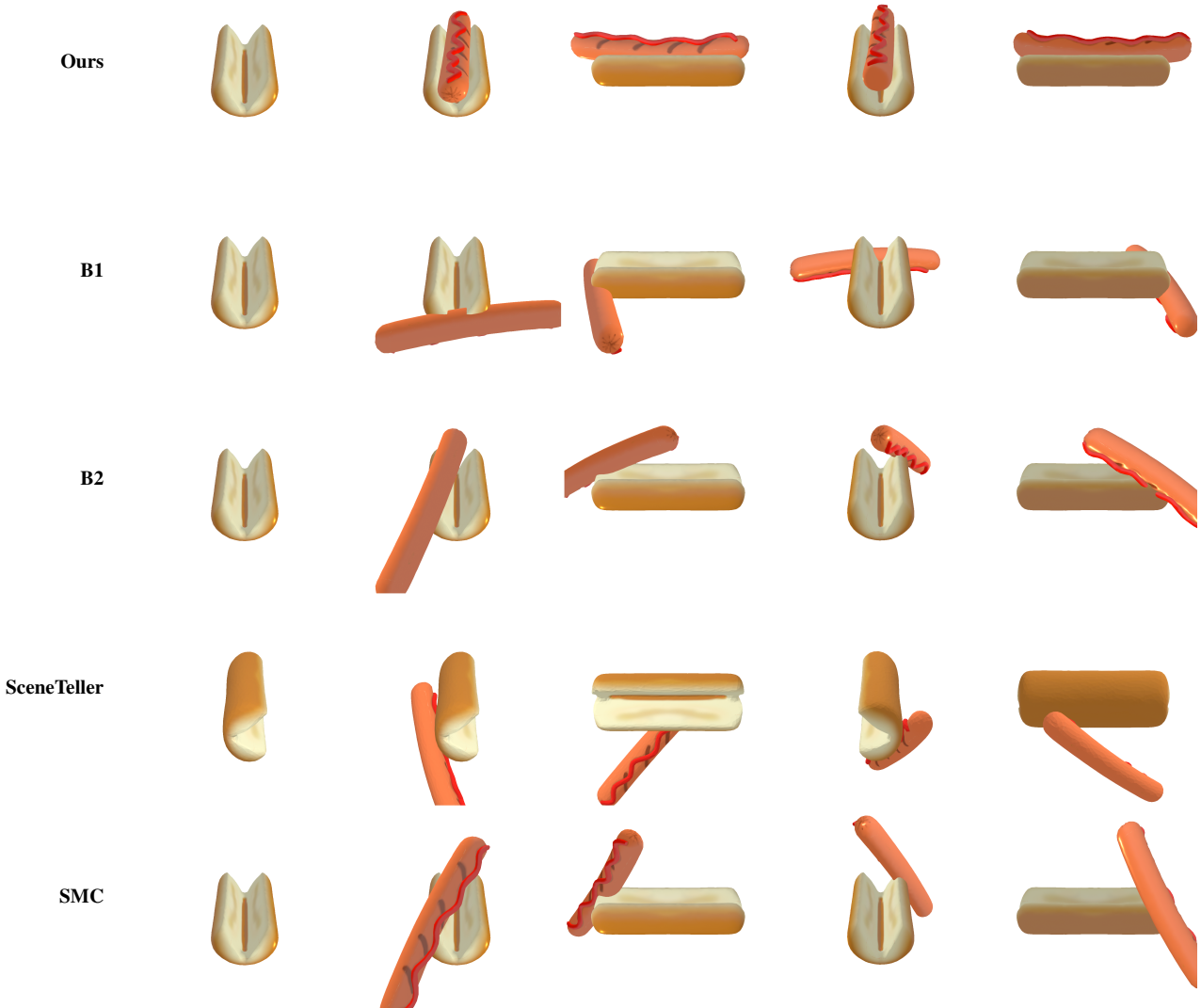


Figure 19. **Per-mesh qualitative comparison: hot dog and bun.** Rows correspond to our method, B1, B2, SceneTeller, and SMC (top to bottom). In each row, the leftmost panel shows the target mesh alone, followed by the final aligned meshes rendered from four different viewing angles. Only our method produces a physically plausible configuration where the sausage rests inside the bun; B2 and SMC place the hot dog above the bun, but it floats without realistic contact.

“Man wearing a cowboy hat”



Figure 20. **Per-mesh qualitative comparison: man and cowboy hat.** Rows correspond to our method, B1, B2, SceneTeller, and SMC (top to bottom). In each row, the leftmost panel shows the target mesh alone, followed by the final aligned meshes rendered from four different viewing angles. Our method positions the hat stably on the head; although B2, SMC, and SceneTeller place the hat close to the man’s head, their configurations remain physically implausible, with poor contact or penetration.

“Chocolate box with a half-open lid on top”

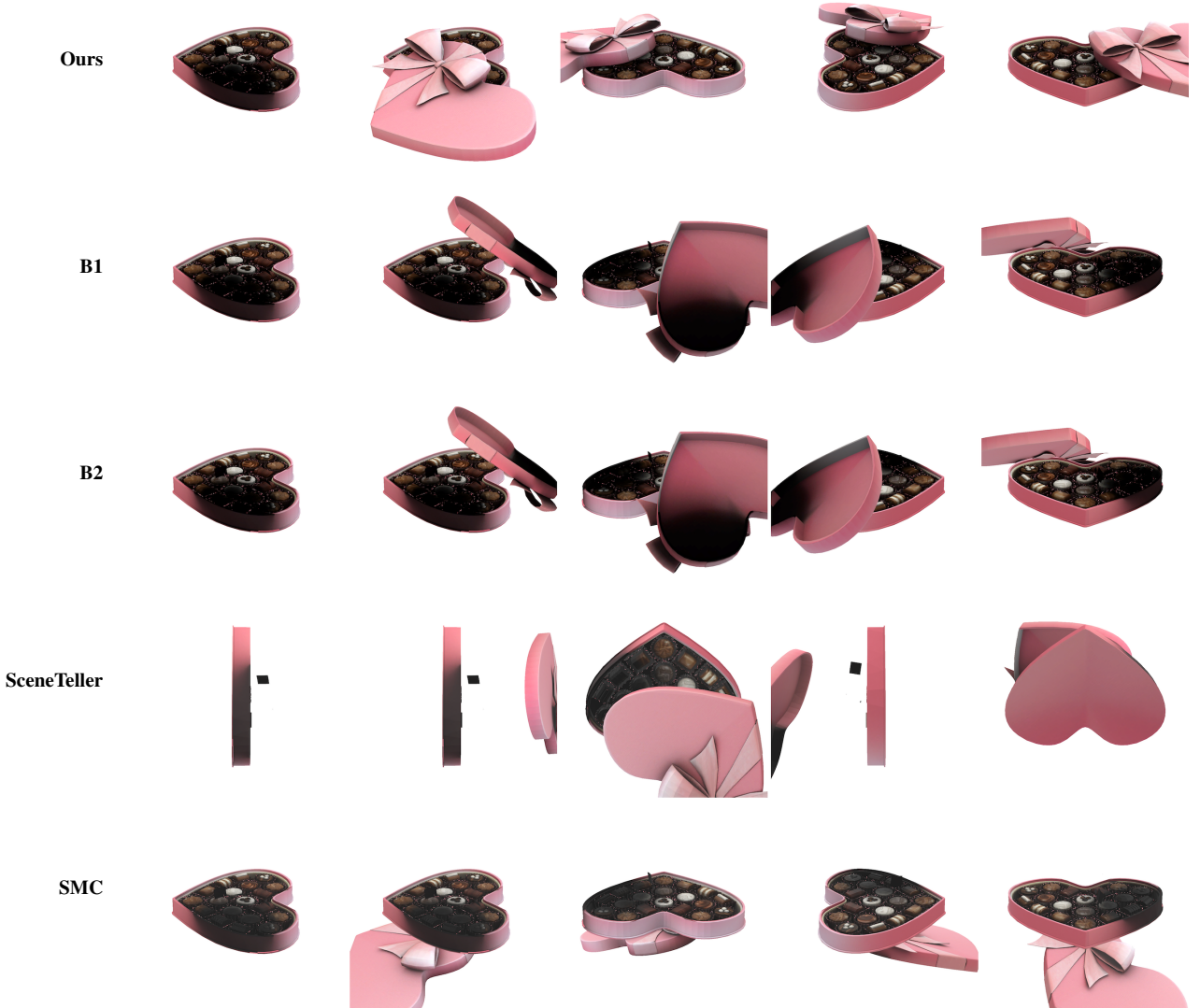


Figure 21. **Per-mesh qualitative comparison: chocolate box and lid.** Rows correspond to our method, B1, B2, SceneTeller, and SMC (top to bottom). In each row, the leftmost panel shows the target mesh alone, followed by the final aligned meshes rendered from four different viewing angles. Only our result matches the prompt with a half-open lid resting on the box; in B1 and B2 the lid appears upside down, in SceneTeller it floats above the box, and in SMC it is placed below the box rather than on top.

“Judge’s gavel on its base”

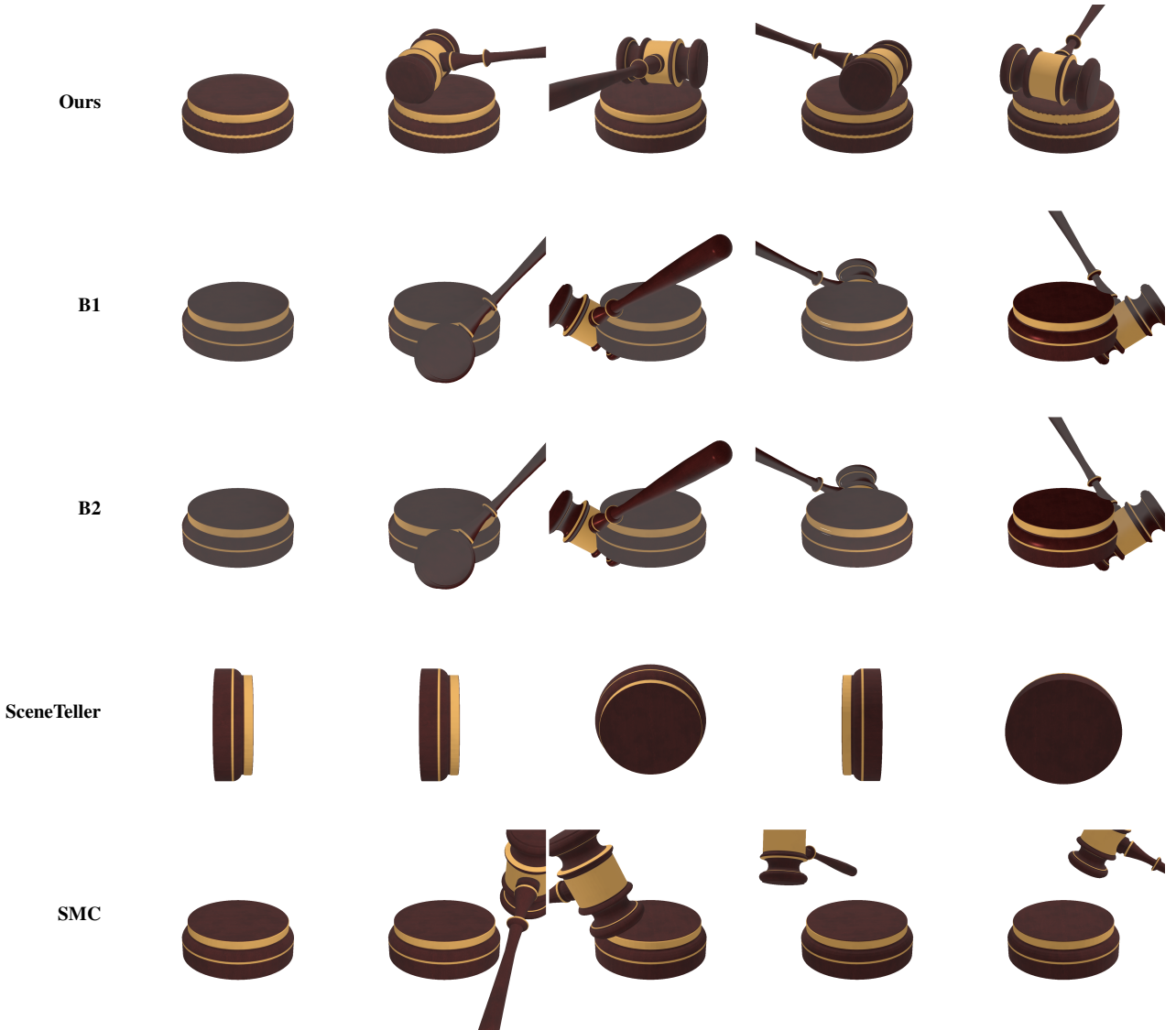


Figure 22. **Per-mesh qualitative comparison: judge’s gavel and base.** Rows correspond to our method, B1, B2, SceneTeller, and SMC (top to bottom). In each row, the leftmost panel shows the target mesh alone, followed by the final aligned meshes rendered from four different viewing angles. Our method places the gavel directly and stably on its base; in B1 and B2 the gavel misses the base. Scene teller place the gavel far away from it’s base, and in SMC the configuration can look text-aligned from some views but the gavel is not actually resting above the base.

“Toothpaste sits on top of toothbrush bristles”

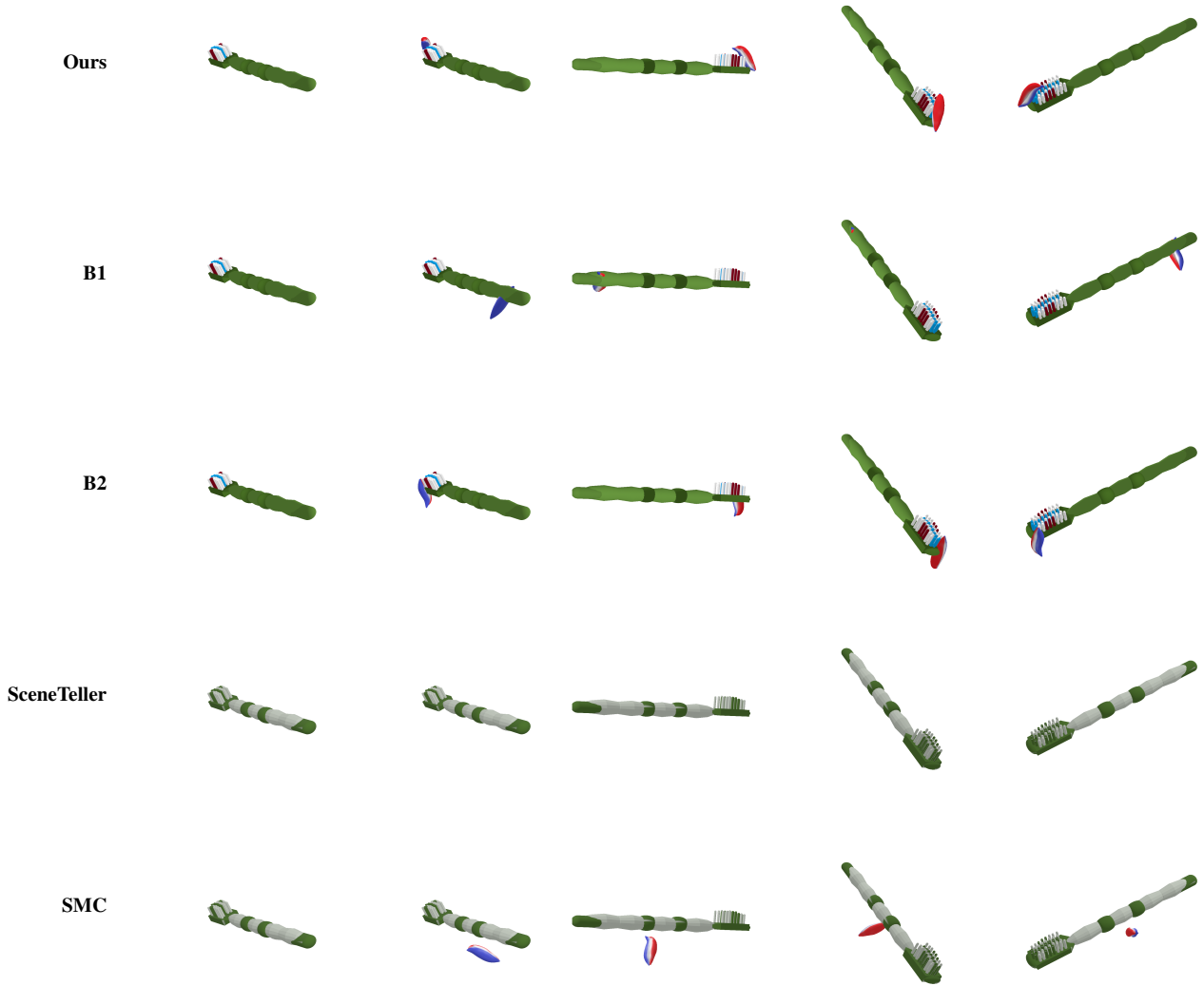


Figure 23. **Per-mesh qualitative comparison: toothpaste and toothbrush.** Rows correspond to our method, B1, B2, SceneTeller, and SMC (top to bottom). In each row, the leftmost panel shows the target mesh alone, followed by the final aligned meshes rendered from four different viewing angles. While not perfect, our method yields a physically plausible placement of the toothpaste on the bristles. B2 comes close to placing it on top but still produces a floating, non-physical configuration.

“Queen of hearts wearing a golden crown”



Figure 24. **Per-mesh qualitative comparison: queen and crown.** Rows correspond to our method, B1, B2, SceneTeller, and SMC (top to bottom). In each row, the leftmost panel shows the target mesh alone, followed by the final aligned meshes rendered from four different viewing angles. In our result, the crown sits directly and stably on the queen’s head; in the other baselines the crown is either far from the head, or even not clearly visible in the final view.